PHYSICAL REVIEW B **97**, 115421 (2018)

Time-varying metamaterials based on graphene-wrapped microwires: Modeling and potential applications

Mohammad Mahdi Salary, Samad Jafar-Zanjani, and Hossein Mosallaei[*]

Metamaterials Lab, Electrical and Computer Engineering Department, Northeastern University, Boston, Massachusetts 02115, USA

(Received 2 January 2018; revised manuscript received 23 January 2018; published 15 March 2018)

The successful realization of metamaterials and metasurfaces requires the judicious choice of constituent elements. In this paper, we demonstrate the implementation of time-varying metamaterials in the terahertz frequency regime by utilizing graphene-wrapped microwires as building blocks and modulation of graphene conductivity through exterior electrical gating. These elements enable enhancement of light-graphene interaction by utilizing optical resonances associated with Mie scattering, yielding a large tunability and modulation depth. We develop a semianalytical framework based on transition-matrix formulation for modeling and analysis of periodic and aperiodic arrays of such time-varying building blocks. The proposed method is validated against full-wave numerical results obtained using the finite-difference time-domain method. It provides an ideal tool for mathematical synthesis and analysis of space-time gradient metamaterials, eliminating the need for computationally expensive numerical models. Moreover, it allows for a wider exploration of exotic space-time scattering phenomena in time-modulated metamaterials. We apply the method to explore the role of modulation parameters in the generation of frequency harmonics and their emerging wavefronts. Several potential applications of such platforms are demonstrated, including frequency conversion, holographic generation of frequency harmonics, and spatiotemporal manipulation of light. The presented results provide key physical insights to design time-modulated functional metadevices using various building blocks and open up new directions in the emerging paradigm of time-modulated metamaterials.

DOI: 10.1103/PhysRevB.97.115421

Metamaterials, composed of subwavelength engineered building blocks, provide great flexibility in the manipulation of light waves and fields by providing access to a wider design space beyond naturally available materials [1]. In particular, a great amount of attention has been given to two-dimensional metamaterials, or metasurfaces, due to their low profile, which makes them more favorable in terms of fabrication and allows shrinking the size of optical platforms [2]. The operation of metamaterials and metasurfaces relies predominantly on the realization of a gradient index profile [3] or a gradient discontinuity in the phase and amplitude [4]. These design principles have been used in a variety of flat and bulk optical components for different applications, such as focusing [5], bending [6], holography [7], etc.

In conventional designs of metamaterials, the gradient characteristics are achieved through geometrical variation of building blocks, which makes their operation static, tying them to a specific application after fabrication. More recently, several efforts have been made regarding postfabrication control of the metamaterials by exploiting mechanical reconfiguration [8,9], thermal phase transitions [10,11], and electro-optical materials [12–17] in geometrically fixed platforms. Such tunable designs render more flexibility in the operation, allowing for multifunctionality and on-demand manipulation of light.

Despite the real-time tunability offered by reconfigurable metamaterials, their operation has remained mostly quasistatic as the variations in time are disregarded. Exploiting tunability mechanisms also offers the possibility of implementing time-varying metamaterials in which the parameters of the metamaterials are varying in time by changing the external stimuli. Temporal variation enables several exotic scattering phenomena by breaking the time-reversal symmetry and generation of frequency harmonics in the output spectrum [18–29]. It also adds a new dimensionality to the design space, providing even further flexibility in the design, which can be exploited to tackle several challenges associated with static and quasistatic metamaterials and realize novel advanced functionalities.

In the microwave frequency regime, implementation of time-modulated metamaterials has been demonstrated by using lumped elements such as varactors in microstrip circuits [23–26]. Moving beyond microwaves into terahertz (THz) and infrared (IR) frequencies, several mechanisms can be foreseen for the synthesis of time-varying metamaterials by utilizing different trigger mechanisms, such as, mechanical actuation, thermal phase transition, and electrical gating. Among all these mechanisms, electrical gating of electro-optical materials holds the greatest promise as it offers a continuous tunability range and has the quickest response time, allowing for larger modulation frequencies. Graphene has been shown to be an ideal candidate for electro-optical tunability in the THz and IR frequency regimes due to its many advantages, including low loss, low dimensionality, broadband tunability, large-scale fabrication feasibility, and interface compatibility with silicon

---

[*] hosseinm@ece.neu.edu

2469-9950/2018/97(11)/115421(14)

fabrication technology. The surface carrier concentration of a graphene layer can be changed by applying an exterior gate voltage in a parallel capacitor configuration, which results in a change in the surface conductivity. Graphene has been incorporated into many active optical platforms for different applications, such as tuning the optical absorption [17] and phase modulation of reflected light [13]. In such designs, graphene is integrated into resonant geometries that enhance the light-graphene interaction, yielding a larger tunability. The surface conductivity of graphene can be modulated with frequencies up to several gigahertz (GHz) [30–34]. As such, graphene-integrated building blocks can be used to implement electrically tunable time-modulated metamaterials in THz and IR frequencies by utilizing a radiofrequency (RF) biasing network.

Along with the progress in materials technology, which allows realization of time-varying metamaterials, there is a need for simulation techniques to design and analyze such emerging platforms and unravel the novel physics associated with light scattering from time-varying metamaterials. The finite-difference time-domain (FDTD) method can be conveniently used as it can easily take into account the variation of material parameters in time. However, it lacks efficiency to model arrays of large area with subwavelength features as it requires the discretization of a whole computational domain in space and time, which leads to numerical models featuring a large number of degrees of freedom. Introducing time variations adds yet another challenge for FDTD simulations. In particular, modulation frequencies of the materials that are accessible in practice are small compared to operating frequencies at IR and THz frequency regimes. As such, the FDTD method requires an enormous number of time steps to capture steady-state solutions, which becomes very time-consuming and requires tremendous computational resources. Therefore, developing semianalytical techniques capable of modeling time-varying elements offers great benefits as they do not suffer from numerical inaccuracies inherent within the FDTD method, and they enable fast design of time-varying metamaterials. Furthermore, they can provide more physical insight into the scattering phenomena.

The objective of this paper is threefold: (a) implementation of time-varying metamaterials in the THz frequency regime based on graphene-wrapped microwires, (b) developing a robust semianalytical framework for rigorous modeling of such structures, and (c) investigating unexplored potential applications of time-modulated metamaterials for light manipulation. We demonstrate the realization of time-varying metamaterials in the THz frequencies by adopting graphene-wrapped microwires as building blocks and modulating the surface conductivity of graphene via RF signals. Such elements can enhance light-graphene interactions through resonant features associated with Mie scattering, yielding comparable modulation depths with planar structures of much greater volume. Furthermore, these elements exhibit a strong gate dependence and reduced subthreshold swing due to their large aspect ratios [35,36]. Graphene-wrapped wires have been fabricated via chemical-vapor-deposition (CVD) growth of monolayer graphene on microwires [37,38] and draping graphene flakes over microwires with an adhesive tape [39]. They have been envisioned for a variety of applications, such as tunable modulation of absorption [40], cloaking [41], wave guiding [42], nonlinear harmonic generation [43], etc. We develop a robust semianalytical framework for the analysis of such time-varying elements based on a transition-matrix (T-matrix) formulation. The method is able to accurately characterize both near-field and far-field responses of periodic and aperiodic arrangements of the elements on top of a substrate. The validity of the method is rigorously verified by comparing the results obtained with FDTD simulations. An enormous computational gain is afforded by the proposed method, which can be used for the fast design of time-varying metamaterials and metasurfaces with advanced functionalities by avoiding computationally expensive numerical models. We apply the method to explore several potential applications of time-modulated metamaterial platforms for light manipulation. The frequency conversion process in the time-modulated building blocks is studied, and its dependence on the resonant characteristics of the element is analyzed. We also analyze the effects of modulation parameters on the amplitude and phase of generated frequency harmonics in time-modulated metasurfaces. It is revealed that an independent control over the phase and amplitude of scattered frequency harmonics can be achieved by controlling the modulation phase delay and the modulation depth, enabling high-efficiency holography. Furthermore, we demonstrate that the effective refractive index of deeply subwavelength microwires can be modulated in time to realize time-modulated metamaterials offering spatiotemporal control of light. In particular, a time-modulated lens is designed in which the bending angle varies with time enabling ultrafast beam scanning. The rest of this paper is organized as follows. In Sec. I, the development of a semianalytical technique is detailed. Then, the method is validated by comparing the near-field results against full-wave FDTD simulations in Sec. II. In Sec. III, we utilize the method to establish design rules for novel functional time-modulated metamaterial platforms. Finally, the conclusions are drawn in Sec. IV.

I. FORMULATION

There have been several efforts in analytical modeling of electromagnetic scattering from time-varying structures [18–24]. However, all of those efforts dealt with space-time modulated slabs or impedance surfaces with relatively simple periodic space-time gradients for effective constituent parameters that rely on homogenization and provide no clue about implementation. The homogenization approach becomes unreliable for aperiodic structures or when constituent elements are resonant and not deeply subwavelength. Furthermore, this approach is not applicable to metadevices with arbitrary arrangements of time-modulated building blocks driven by different modulation parameters. Here, we aim at developing a robust semianalytical method capable of modeling space-time gradient metamaterials consisting of periodic and aperiodic arrangement of microwires wrapped by time-varying graphene layers. Our method avoids the limitations associated with prior analytic homogenization techniques.

The available geometrical features of a scatterer allow us to study electromagnetic scattering analytically using different techniques relying on multipole expansion of the fields. Among the various multipole scattering techniques, the T-matrix method is the most powerful due to its simplicity and

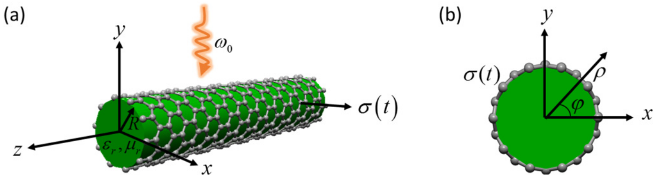

FIG. 1. The schematic of an isolated microwire wrapped by time-varying graphene.

generality. The T-matrix method was introduced by Waterman [44] for electromagnetic scattering from an arbitrarily shaped homogeneous scatterer. The formulation was extended by Peterson and Strom to the case of an arbitrary number of two-dimensional (2D) scatterers by applying the translation formula to the cylindrical wave solution of Helmoltz's wave equation [45]. The method has evolved quite dramatically ever since and has been adapted to solve several problems involving periodic and aperiodic arrangements of cylindrical objects [46–49]. In particular, the authors have extended the method to take into account multiple scattering between cylinders and layered substrates [50] as well as crossed configurations of cylinders [51,52]. Here, we develop a semianalytic framework by extending the T-matrix formulation to solve electromagnetic scattering from substrate-supported periodic and aperiodic arrays of cylindrical structures wrapped by time-varying graphene layers. In the following, we establish the matrix equations for electromagnetic scattering of multipoles corresponding to different frequency harmonics generated by time-varying elements similar to the definition of the T-matrix for time-varying acoustic materials [53]. Further details regarding the block structure of the matrices and building the matrix equations can be found in Sec. 1 of the Supplemental Material [54].

A. T-matrix of an isolated time-varying graphene-wrapped wire

We begin developing the formulation by obtaining the T-matrix of an isolated wire element wrapped by a time-varying isotropic graphene layer located in free space, as shown in Fig. 1(a). The radius, relative permittivity, and relative permeability of the core are denoted by R, ϵ_c, and μ_c, respectively. The graphene layer is characterized by a time-varying surface conductivity of $\sigma(\omega_0,t)$, which is dependent on the excitation frequency (ω_0). The coordinate system is chosen such that z axis lies along the microwire axis while the origin is located at the center of the microwire. (ρ,ϕ) are polar coordinates of the frame as shown in Fig. 1(b). First, we consider a plane-wave incidence with transverse magnetic (TM$_z$) polarization where the electric field is along the microwire axis. We assume the temporal variations are small compared with oscillations of excitation frequency such that the dispersion effects induced by time modulation can be ignored. The validity of this assumption is ensured by the range of accessible modulation frequencies for electro-optical materials in the THz and IR frequency regimes. As such, the constitutive relations can be written in multiplicative form in the time domain for each excitation frequency. It should be remarked that while disregarding the modulation-induced dispersion effects, we consider the dependency of conductivity temporal variations to excitation frequency, thus considering strong material dispersion in these frequency regimes. In this case, the boundary conditions at the interface of the microwire ($\rho = R$) can be written as follows in the time domain [55]:

$$\hat{\rho} \times [\vec{E}_{iz}(t) + \vec{E}_{sz}(t) - \vec{E}_{cz}(t)] = 0, \tag{1}$$

$$\hat{\rho} \times [\vec{H}_{i\phi}(t) + \vec{H}_{s\phi}(t) - \vec{H}_{c\phi}(t)] = \sigma(\omega_0,t)\vec{E}_{cz}(t), \tag{2}$$

where $\vec{E}$ and $\vec{H}$ are electric and magnetic fields, respectively, and the subscripts i, s, and c correspond to the incident, scattered, and internal field contributions, respectively. According to the multipole expansion of the fields, they can be expressed as a summation of orthogonal cylindrical wave functions in the frequency domain. Therefore, the time-domain representation of the electric-field contributions can be written as the inverse Fourier transforms of the multipole expansions:

$$\vec{E}_{iz}(t) = \frac{1}{2\pi}\int \sum_{m=-\infty}^{+\infty} A_m(\omega) J_m\left(\frac{\omega}{c}\rho\right) e^{(im\phi)} e^{(i\omega t)} d\omega, \tag{3}$$

$$\vec{E}_{sz}(t) = \frac{1}{2\pi}\int \sum_{m=-\infty}^{+\infty} B_m(\omega) H_m\left(\frac{\omega}{c}\rho\right) e^{(im\phi)} e^{(i\omega t)} d\omega, \tag{4}$$

$$\vec{E}_{cz}(t) = \frac{1}{2\pi}\int \sum_{m=-\infty}^{+\infty} C_m(\omega) J_m\left(\frac{n_c\omega}{c}\rho\right) e^{(im\phi)} e^{(i\omega t)} d\omega, \tag{5}$$

where ω is the angular frequency, c is the speed of light in vacuum, and $n_c = \sqrt{\epsilon_c \mu_c}$ is the refractive index of the core. $J_m(\cdot)$ and $H_m(\cdot)$ are the Bessel and Hankel functions of the first kind and order m. $A_m(\omega)$, $B_m(\omega)$, and $C_m(\omega)$ are the unknown coefficients of the multipole expansions of the fields. Similarly, the ϕ-component of the magnetic-field contributions can be obtained using $\vec{H}_\phi = -\frac{1}{i\omega\mu_0}\frac{\partial \vec{E}_z}{\partial \rho}$, as

$$\vec{H}_{i\phi}(t) = \frac{i}{2\pi\mu_0 c}\int \sum_{m=-\infty}^{+\infty} A_m(\omega) J_m'\left(\frac{\omega}{c}\rho\right) e^{(im\phi)} e^{(i\omega t)} d\omega, \tag{6}$$

$$\vec{H}_{s\phi}(t) = \frac{i}{2\pi\mu_0 c}\int \sum_{m=-\infty}^{+\infty} B_m(\omega) H_m'\left(\frac{\omega}{c}\rho\right) e^{(im\phi)} e^{(i\omega t)} d\omega, \tag{7}$$

$$\vec{H}_{c\phi}(t) = \frac{in_c}{2\pi\mu_0 c}\int \sum_{m=-\infty}^{+\infty} C_m(\omega) J_m'\left(\frac{n_c\omega}{c}\rho\right) e^{(im\phi)} e^{(i\omega t)} d\omega, \tag{8}$$

where μ_0 is the free-space permeability and the prime denotes derivative with respect to ρ. Substituting field representation (3)–(5) into boundary condition (1) and using the orthogonality of exponential functions of $e^{im\phi}$ and $e^{i\omega t}$, it can be easily obtained that

$$C_m(\omega) = \frac{A_m(\omega) J_m\left(\frac{\omega}{c}R\right) + B_m(\omega) H_m\left(\frac{\omega}{c}R\right)}{J_m\left(\frac{n_c\omega}{c}R\right)}. \tag{9}$$

For treating boundary condition (2), we rewrite the time-domain multiplication in the right-hand side of the equation as the inverse Fourier transform of the convolution in the frequency domain as

$$\begin{aligned}
&\frac{1}{2\pi}\mathscr{F}_{\omega}^{-1}\left[\hat{\sigma}_0(\omega) * \sum_{m=-\infty}^{+\infty} C_m(\omega) J_m\left(\frac{n_c\omega}{c}\rho\right) e^{(im\phi)}\right] \\
&= \frac{1}{2\pi}\mathscr{F}_{\omega}^{-1}\left[\int \hat{\sigma}_0(\omega-\omega') \sum_{m=-\infty}^{+\infty} C_m(\omega') J_m\right. \\
&\quad \left.\times \left(\frac{n_c\omega'}{c}\rho\right) e^{(im\phi)} d\omega'\right] \\
&= \frac{1}{4\pi^2}\iint \hat{\sigma}_0(\omega-\omega') \sum_{m=-\infty}^{+\infty} C_m(\omega') J_m \\
&\quad \times \left(\frac{n_c\omega'}{c}\rho\right) e^{(im\phi)} d\omega' e^{(i\omega t)} d\omega, \qquad (10)
\end{aligned}$$

where $\mathscr{F}^{-1}$ denotes inverse Fourier transform and $\hat{\sigma}_0(\omega)$ is the Fourier transform of $\sigma(\omega_0,t)$ with respect to t. Now, using the field representations (6)–(8) and (10), the boundary condition (2) will result in the following equation, according to the orthogonality of exponential functions $e^{im\phi}$ and $e^{i\omega t}$:

$$\begin{aligned}
&A_m(\omega) J_m'\left(\frac{\omega}{c}R\right) + B_m(\omega) H_m'\left(\frac{\omega}{c}R\right) - n_c C_m(\omega) J_m'\left(\frac{n_c\omega}{c}R\right) \\
&- \frac{i\mu c}{2\pi}\int \hat{\sigma}_0(\omega-\omega') C_m(\omega') J_m\left(\frac{n_c\omega'}{c}R\right) d\omega' = 0. \qquad (11)
\end{aligned}$$

To build the T-matrix, we are looking for an equation that relates $A_m(\omega)$ to $B_m(\omega)$. Substituting (9) into (11), we will arrive at

$$\begin{aligned}
&A_m(\omega)\left[J_m'\left(\frac{\omega}{c}R\right) - n_c J_m\left(\frac{\omega}{c}R\right)\frac{J_m'\left(\frac{n_c\omega}{c}R\right)}{J_m\left(\frac{n_c\omega}{c}R\right)}\right] \\
&\quad + \frac{icn_c\mu}{2\pi}\int \hat{\sigma}_0(\omega-\omega') A_m(\omega') J_m\left(\frac{\omega'}{c}R\right)\frac{J_m(\frac{\omega'}{c}R)}{J_m(\frac{n_c\omega'}{c}R)} d\omega' \\
&= B_m(\omega)\left[n_c H_m\left(\frac{\omega}{c}R\right)\frac{J_n'\left(\frac{n_c\omega}{c}R\right)}{J_m\left(\frac{n_c\omega}{c}R\right)} - H_m'\left(\frac{\omega}{c}R\right)\right] \\
&\quad - \frac{icn_c\mu}{2\pi}\int \hat{\sigma}_0(\omega-\omega') B_m(\omega') H_m\left(\frac{\omega'}{c}R\right)\frac{J_m(\frac{\omega'}{c}R)}{J_m(\frac{n_c\omega'}{c}R)} d\omega'. \qquad (12)
\end{aligned}$$

The above integral equation implies that a monochromatic $A_m(\omega)$ will excite a continuous spectrum of frequency harmonics $B_m(\omega')$ in the output. The equation can be discretized with a specific frequency resolution $\Delta\omega$ to obtain the T-matrix. Choosing $\omega = \omega_p = \omega_0 + p\Delta\omega$ and $\omega' = \omega_q = \omega_0 + q\Delta\omega$, we will arrive at the T-matrix of a wire wrapped by time-varying graphene as $\overline{\overline{T}} = [\overline{\overline{T}}]_{mn}^{qp}$ with $m,n,p,q = \ldots,-1,0,+1,\ldots,$ whose elements are given in (13).

$[\overline{\overline{T}}]_{mn}^{qp}$ is the T-matrix element that relates the pth frequency harmonic corresponding to the nth cylindrical mode of the incident field to the qth frequency harmonic corresponding to the mth cylindrical mode of the scattered field. Due to the δ_{mn} term in Eq. (13), it can be understood that the cylindrical modes are decoupled similar to the static case. Therefore, for each cylindrical mode, Eq. (13) will result in a matrix division whose solution gives a matrix relating the incident and scattered frequency harmonics corresponding to that cylindrical mode.

For the transverse electric polarization where the magnetic field is along the microwire axis (TE$_z$), we can follow the same procedure by writing the time-domain representation of $\vec{H}_z$ and $\vec{E}_\phi$ field contributions as the inverse Fourier transform of their corresponding multipole expansions. Treating the boundary conditions for these field components in a similar fashion will result in the T-matrix for TE polarization whose elements are given in (14).

Setting $\hat{\sigma}_0(\omega_p - \omega_q) = 0$, Eqs. (13) and (14) will result in the T-matrices of an isolated microwire without any graphene coating [47]. Moreover, setting $\hat{\sigma}_0(\omega_p - \omega_q) = 2\pi\delta_{pq}\sigma(\omega_0)$ will yield the T-matrices of a microwire coated by a time-invariant graphene layer, which verifies the validity of our formulation in the static limit [55].

It is important to mention that for a periodic modulation in time with a modulation frequency of ω_m, the Fourier spectrum of $\sigma(\omega_0,t)$ becomes discrete and can be written as $\hat{\sigma}_0(\omega) = \sum_s P^s\delta(\omega - s\omega_m)$. This implies that the output spectrum will be discrete as well and the generated frequency harmonics will consist of the excitation frequency up- and down-modulated by the modulation frequency. In this case, one can choose $\Delta\omega = \omega_m$ for discretization of the T-matrix equation and replace $\hat{\sigma}_0(\omega_p - \omega_q)$ by $P^{(p-q)}$ in Eqs. (13) and (14). The modulation-induced dispersion effects in self-couplings and mutual couplings can be taken into account approximately by considering the dependence of the Fourier spectrum of conductivity to input frequencies ω_p in the matrix equation.

TM polarization:

$$[\overline{\overline{T}}]_{mn}^{qp} = \delta_{mn}\frac{J_n'\left(\frac{\omega_p}{c}R\right)J_n\left(\frac{n_c\omega_p}{c}R\right)\delta_{pq} - n_c J_n\left(\frac{\omega_p}{c}R\right)J_n'\left(\frac{n_c\omega_p}{c}R\right)\delta_{pq} + \frac{ic\mu_0}{2\pi}\hat{\sigma}_0(\omega_p-\omega_q)J_n\left(\frac{n_c\omega_q}{c}R\right)J_n\left(\frac{\omega_q}{c}R\right)}{-H_n'\left(\frac{\omega_p}{c}R\right)J_n\left(\frac{n_c\omega_p}{c}R\right)\delta_{pq} + n_c H_n\left(\frac{\omega_p}{c}R\right)J_n'\left(\frac{n_c\omega_p}{c}R\right)\delta_{pq} - \frac{ic\mu_0}{2\pi}\hat{\sigma}_0(\omega_p-\omega_q)J_n\left(\frac{n_c\omega_q}{c}R\right)H_n\left(\frac{\omega_q}{c}R\right)}. \qquad (13)$$

TE polarization:

$$[\overline{\overline{T}}]_{mn}^{qp} = \delta_{mn}\frac{J_n'\left(\frac{n_c\omega_p}{c}R\right)J_n\left(\frac{\omega_p}{c}R\right)\delta_{pq} - n_c J_n\left(\frac{n_c\omega_p}{c}R\right)J_n'\left(\frac{\omega_p}{c}R\right)\delta_{pq} - \frac{i}{2\pi\epsilon_0 c}\hat{\sigma}_0(\omega_p-\omega_q)J_n'\left(\frac{n_c\omega_q}{c}R\right)J_n'\left(\frac{\omega_q}{c}R\right)}{-H_n\left(\frac{\omega_p}{c}R\right)J_n'\left(\frac{n_c\omega_p}{c}R\right)\delta_{pq} + n_c H_n'\left(\frac{\omega_p}{c}R\right)J_n\left(\frac{n_c\omega_p}{c}R\right)\delta_{pq} + \frac{i}{2\pi\epsilon_0 c}\hat{\sigma}_0(\omega_p-\omega_q)J_n'\left(\frac{n_c\omega_q}{c}R\right)H_n'\left(\frac{\omega_q}{c}R\right)}. \qquad (14)$$

The T-matrix for a multimaterial wire consisting of several dielectric and graphene layers can be obtained by generalizing the T-matrix obtained here using an aggregate T-matrix [49] approach, which is presented in Sec. 2 of the Supplemental Material [54].

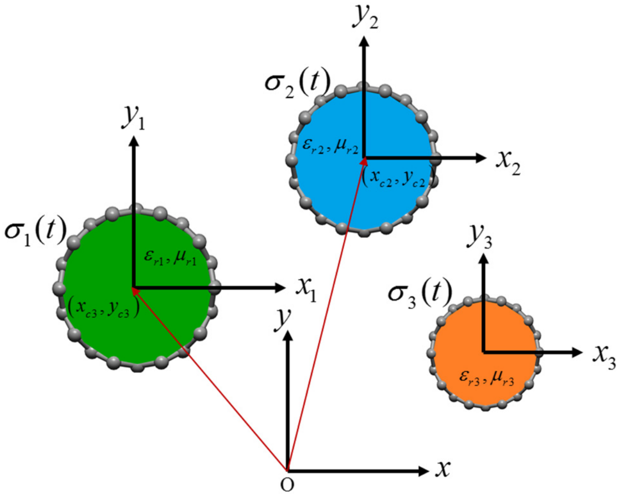

FIG. 2. The schematic of an aperiodic arrangement of microwires wrapped by time-varying graphene layers.

B. Aperiodic array of time-varying wires

Next, we consider an aperiodic array of N graphene-wrapped wires that can have different sizes, different materials, and different time-variation profiles for the conductivity of graphene layers, as shown in Fig. 2. We introduce N local coordinate systems located at the centers of N wires, with (x_l,y_l) and (ρ_l,ϕ_l) denoting the Cartesian and polar coordinates of the frame corresponding to the lth wire, respectively. The vector pointing from the origin of the global coordinate system to the center of the lth wire is defined as $\vec{r}_l = (x_{cl},y_{cl},0)$, as shown in Fig. 2.

The scattered fields from each wire can be expressed as a summation of multipole expansions with different frequency harmonics in its corresponding local coordinate system. For the TM polarization, the scattered electric field from the lth microwire can be written as

$$\vec{E}^{l}_{sz} = \sum_{p=-\infty}^{+\infty}\sum_{m=-\infty}^{+\infty} {}^{p}_{m}B_l H_m\left(\frac{\omega_p}{c}\rho_l\right)e^{im\phi_l}, \tag{15}$$

where ${}^{p}_{m}B_l$ is the scattering coefficient of the lth microwire corresponding to the mth cylindrical mode and the pth frequency harmonic and $\omega_p = \omega_0 + p\Delta\omega$. A similar equation can be written for $\vec{H}_{sz}$ in the case of TE polarization. Using Graf's addition theorem, each cylindrical mode of the scattered field in the local coordinates of the lth microwire can be translated to an expansion of cylindrical modes of incident field in the local coordinates of the kth microwire as [46]

$$H_m\left(\frac{\omega_p}{c}\rho_l\right)e^{im\phi_l} = \sum_{n=-\infty}^{+\infty}\alpha_{mn}(\vec{r}_k,\vec{r}_l)J_n\left(\frac{\omega_p}{c}\rho_k\right)e^{in\phi_k}, \tag{16}$$

where $\alpha_{mn}(\vec{r}_k,\vec{r}_l)$ is the translation coefficient of cylindrical harmonics and is given as [46]

$$\alpha_{mn}(\vec{r}_k,\vec{r}_l) = H_{m-n}\left(\frac{\omega_p}{c}d_{l,k}\right)e^{i(n-m)\phi_{l,k}}, \tag{17}$$

where $d_{l,k} = \sqrt{(y_{cl}-y_{ck})^2+(x_{cl}-x_{ck})^2}$ and $\phi_{l,k} = \arctan2(y_{cl}-y_{ck},x_{cl}-x_{ck})$. Following the block structure of the T-matrix, a translation matrix can be defined as $\overline{\overline{\alpha}}(\vec{r}_k,\vec{r}_l) = [\overline{\overline{\alpha}}(\vec{r}_k,\vec{r}_l)]^{qp}_{mn}$, whose element relates the pth frequency harmonic corresponding to the nth cylindrical mode of the incident field to the qth frequency harmonic corresponding to the mth cylindrical mode of the scattered field. Due to the decoupling of frequency harmonics in translation of cylindrical modes, $\alpha^{qp}_{mn}(\vec{r}_k,\vec{r}_l) = \delta_{qp}\alpha_{mn}(\vec{r}_k,\vec{r}_l)$.

Denoting the isolated T-matrix of the lth microwire as $\overline{\overline{T}}_l$, it can be written as

$$\overline{B}_l = \overline{\overline{T}}_l\left(\overline{A}_l + \sum_{\substack{k=1\\k\neq l}}^{N}\overline{\overline{\alpha}}(\vec{r}_l,\vec{r}_k)\overline{B}_k\right). \tag{18}$$

Writing the same coupling equation for all N microwires, we will arrive at the following system of equations whose solution gives the unknown scattering coefficients of each microwire:

$$\begin{bmatrix} (\overline{\overline{T}}_1)^{-1} & -\overline{\overline{\alpha}}(\vec{r}_1,\vec{r}_2) & \cdots & -\overline{\overline{\alpha}}(\vec{r}_1,\vec{r}_N) \\ -\overline{\overline{\alpha}}(\vec{r}_2,\vec{r}_1) & (\overline{\overline{T}}_2)^{-1} & \cdots & -\overline{\overline{\alpha}}(\vec{r}_2,\vec{r}_N) \\ \vdots & \vdots & \ddots & \vdots \\ -\overline{\overline{\alpha}}(\vec{r}_N,\vec{r}_1) & -\overline{\overline{\alpha}}(\vec{r}_N,\vec{r}_2) & \cdots & (\overline{\overline{T}}_N)^{-1} \end{bmatrix}\begin{bmatrix}\overline{B}_1\\ \overline{B}_2\\ \vdots\\ \overline{B}_N\end{bmatrix} = \begin{bmatrix}\overline{A}_1\\ \overline{A}_2\\ \vdots\\ \overline{A}_N\end{bmatrix}. \tag{19}$$

In the above equation, $\overline{A}_l$ is the vector of coefficients corresponding to the multipole expansion of the incident field in the local coordinates of the lth microwire. Similar equations can be obtained for TE polarization simply by replacing the TM T-matrix with the TE counter.

In building the T-matrices of the wires with periodic modulations in time, if the modulation frequencies are the same and equal to ω_m, one can choose $\Delta\omega = \omega_m$. Otherwise, in the case of different modulation frequencies, $\Delta\omega$ should be chosen as the greatest common divisor of all modulation frequencies to capture the cross coupling of all frequency harmonics.

C. Periodic array of time-varying wires

Now, let us consider an array of time-varying graphene-wrapped microwires that is periodic along the x-axis direction with a periodicity of Λ as shown in Fig. 3. According to the Floquet theorem [47,48], the scattered field from the array under illumination of a monochromatic plane wave with an excitation frequency of ω_0 and an incidence angle of ϕ_0 can be written as follows for TM polarization:

$$\vec{E}_{sz} = \sum_{l=-\infty}^{+\infty}\sum_{p=-\infty}^{+\infty}\sum_{m=-\infty}^{+\infty} B^{p}_{m}H_m\left(\frac{\omega_p}{c}\rho_l\right)e^{im\phi_l}e^{i\omega_0 l\Lambda\cos(\phi_0)/c} \tag{20}$$

in which the exponential term $e^{i\omega_0 l\Lambda\cos(\phi_0)/c}$ is due to the transverse moment introduced by the oblique incidence. Following

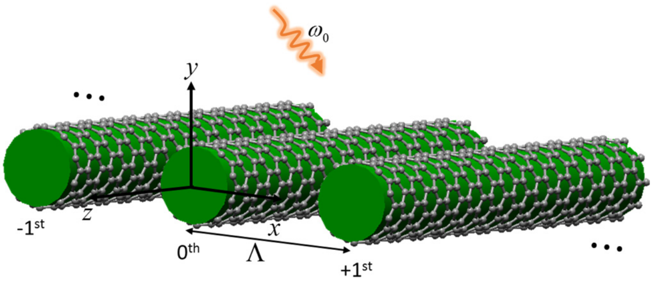

FIG. 3. The schematic of a periodic array of microwires wrapped by time-varying graphene layers.

a similar procedure for the treatment of an aperiodic array, the coupling equation in this case can be written as

$$\overline{B} = \overline{\overline{T}}\left(\overline{A} + \sum_{\substack{l=-\infty \\ l\neq 0}}^{+\infty} \overline{\overline{\alpha}}(\vec{r}_0,\vec{r}_l)e^{i\omega_0 l\Lambda\cos(\phi_0)/c}\overline{B}\right), \tag{21}$$

which leads to

$$\overline{B} = \overline{\overline{T}}\left(\overline{\overline{I}} - \overline{\overline{T}}\sum_{\substack{l=-\infty \\ l\neq 0}}^{+\infty} \overline{\overline{\alpha}}(\vec{r}_0,\vec{r}_l)e^{i\omega_0 l\Lambda\cos(\phi_0)/c}\right)^{-1}\overline{A}. \tag{22}$$

The semi-infinite summations in (22) are called lattice sums, which are slowly convergent. However, they can be efficiently and accurately evaluated using a recurrence formula [48] or a series acceleration technique such as Shank's transformation [51]. Once the unknown scattering coefficients are obtained, the Fourier integral representation of Hankel functions can be used to expand the scattered fields in terms of a summation of reflected and transmitted plane waves [48] over different frequency harmonics and spatial diffraction orders as

$$E^r(x,y) = \sum_{p=-\infty}^{+\infty}\sum_{v=-\infty}^{+\infty} e^{i(k_{xv}x+k_{v,p}y)}\sum_{m=-\infty}^{+\infty} p_{v,p,m}B_m^p, \tag{23}$$

$$E^t(x,y) = \sum_{p=-\infty}^{+\infty}\sum_{v=-\infty}^{+\infty} e^{i(k_{xv}x+k_{v,p}y)}\left(\delta_{v0}\delta_{p0} + \sum_{m=-\infty}^{+\infty} p_{v,p,m}B_m^p\right) \tag{24}$$

with

$$p_{v,p,m} = \begin{cases} \frac{2c^m(-i)^m(k_{xv}+ik_{v,p})^m}{\Lambda k_{v,p}\omega_p^m} & (m \geqslant 0), \\ \frac{2c^{|m|}(i)^{|m|}(k_{xv}-ik_{v,p})^{|m|}}{\Lambda k_{v,p}\omega_p^{|m|}} & (m < 0), \end{cases} \tag{25}$$

$$q_{v,p,m} = \begin{cases} \frac{2c^m(-i)^m(k_{xv}-ik_{v,p})^m}{\Lambda k_{v,p}\omega_p^m} & (m \geqslant 0), \\ \frac{2c^{|m|}(i)^{|m|}(k_{xv}+ik_{v,p})^{|m|}}{\Lambda k_{v,p}\omega_p^{|m|}} & (m < 0), \end{cases} \tag{26}$$

where $k_{xv,p} = -\frac{\omega_0}{c}\cos(\phi_0) + 2v\pi\Lambda$ and $k_{v,p} = \sqrt{\omega_p^2/c^2 - k_{xv}^2}$. In the above equations, v denotes the spatial diffraction order, p denotes the order of the frequency harmonic, and m denotes the cylindrical mode index.

D. Substrate multiple-scattering effects

For a finite aperiodic array, the multiple scattering effects between wires and a layered substrate can be characterized through a reflection matrix whose elements are obtained by evaluating Weyl-type integrals. In this case, the coupling equation (18) can be modified as [50,56]

$$\overline{B}_l = \overline{\overline{T}}_l\left(\overline{A}_l + \sum_{\substack{k=1 \\ k\neq l}}^{k=N} \overline{\overline{\alpha}}(\vec{r}_l,\vec{r}_k)\overline{B}_k + \sum_{k=1}^{k=N} \overline{\overline{RW}}_k\overline{\overline{\beta}}(\vec{r}_l,\vec{r}_k)\overline{B}_k\right), \tag{27}$$

where $\overline{\overline{\beta}}(\vec{r}_l,\vec{r}_k)$ is the matrix of translation coefficients for regular cylindrical harmonics, which can be built similar to $\overline{\overline{\alpha}}(\vec{r}_l,\vec{r}_k)$, and its elements are obtained as [46]

$$\beta_{mn}^{qp}(\vec{r}_l,\vec{r}_k) = \delta_{qp}J_{m-n}\left(\frac{\omega_p}{c}d_{l,k}\right)e^{i(n-m)\phi_{l,k}}. \tag{28}$$

$\overline{\overline{RW}}_k$ is the reflection matrix of the substrate for multipoles of the kth wire whose elements can be expressed as [50]

$$_{mn}^{qp}RW_k = \frac{\delta_{qp}}{2\pi}\int_{-\infty}^{+\infty}\Gamma(\omega_p,n_x)F_{m+n}\left(\frac{2\omega_p}{c}h_k,n_x\right)dn_x \tag{29}$$

in which h_k is the distance of the kth wire from the top interface of the substrate, $\Gamma(\omega_p,n_x)$ is the TM or TE reflection coefficient from the top interface of the substrate corresponding to an angular frequency of ω_p and a tangential wave vector of $k_x = n_x\omega_p/c$, and $F_m(y,n_x)$ is the angular spectrum of scattered cylindrical harmonics, which can be expressed as

$$F_m(y,n_x) = \frac{2e^{i\sqrt{1-n_x^2}y}}{\sqrt{1-n_x^2}}e^{-im\arccos(n_y)}. \tag{30}$$

The integrals in (29) are Weyl-type integrals that can be evaluated efficiently by adopting a numerical integration scheme based on a quadrature algorithm [57,58]. It should be noted that in the presence of a substrate, $\overline{A}_l$ takes into account both incident and reflected fields from the substrate.

For the periodic case, a similar procedure can be adopted. However, it is more convenient to use a scattering matrix approach to obtain reflection and transmission coefficients of the layered system through a recursive formula [48,51] as it does not involve numerical evaluation of Weyl-type integrals.

E. Scope of the method

A block diagram of the procedure for calculation of reflected and transmitted fields in the periodic case and the involved equations is demonstrated in Fig. 4. The procedure for obtaining scattered fields in an aperiodic array is similar, with the governing matrix equation being replaced with (19) and the scattered field being given by (15). Further details regarding technical implementation and assembling of matrices are given in the Supplemental Material [54].

The proposed technique is an analytical treatment of the problem, and it should yield exact results as long as the modulation-induced dispersion effects are negligible, which is guaranteed for the experimentally accessible modulation

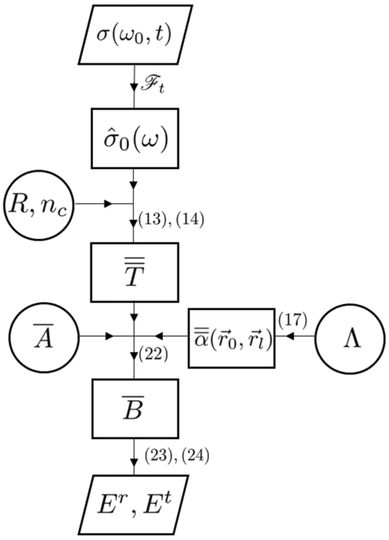

FIG. 4. The block diagram of the steps and equations involved in the calculation of transmitted and reflected fields for a periodic array of wires wrapped by time-modulated graphene layers.

frequencies of electro-optical materials in THz and IR frequencies. The only numerical treatments regarded in the method are a truncation of frequency harmonic and multipole expansions, which can be carried out carefully to ensure the convergence of the results.

Although the T-matrix method developed here is only applicable for modeling wire elements with time-modulated surface conductivities, its application is not limited to only graphene. The active charge accumulation layers in highly doped semiconductors, transparent conducting oxides, and transition-metal nitrides are ultrathin and quasi-2D, which allows them to be modeled with a surface conductivity. The equivalence between 2D and volumetric models is established for modeling graphene layers [59]. It has been shown that an ultrathin volumetric layer with a permittivity of ϵ and a thickness of d is equivalent to a surface conductivity of $\sigma = -i\omega\epsilon_0 d(\epsilon - 1)$.

In the development of this formulation, it has been assumed that the axes of microwires are parallel to each other and the incident plane is perpendicular to the wires axes such that there is no cross-coupling between TE and TM polarizations. The method can be readily extended to the case of crossed wire configurations and out-of-plane incidence using a generalized T-matrix accounting for cross-coupling between orthogonal polarizations [51], which is beyond the focus of this work. Furthermore, the method can be used for any arbitrarily-shaped time-varying 2D scatterer by numerical retrieval of the T-matrix corresponding to different frequency harmonics. An extension to the three-dimensional T-matrix method [60] is also feasible, but we leave it for future research. It should be mentioned that the use of 2D scatterers is preferred in terms of viability as they can be addressed and biased independently without the need for complex three-dimensional grids.

II. VALIDATION

In this section, we rigorously validate the developed semianalytical framework by comparing the near-field results with full-wave FDTD simulations. To this purpose, we consider a dielectric microwire with a radius of $R = 50$ μm and a permittivity of $\epsilon = 3.9$ under normal incidence of a plane wave with an excitation wavelength of $\lambda = 100$ μm. The frequency-dependent conductivity of monolayer graphene is dominated by intraband transitions in the THz regime, which can be expressed as [61]

$$\sigma_{\text{intra}}(\omega) = i\frac{2e^2}{\pi\hbar^2}\frac{k_BT}{\omega+i\tau^{-1}} \times\left(\frac{E_f}{2k_BT}+\ln[1+\exp(-E_f/k_BT)]\right), \tag{31}$$

where e is the electron charge, $\hbar$ is the reduced Planck's constant, k_B is the Boltzmann constant, T is temperature, and τ and E_f are the scattering time and Fermi energy level of graphene, respectively. At room temperature, $k_BT =$ 25.7 meV and $E_f \gg k_BT$ for moderately doped graphene. As such, the conductivity can be approximated as [61]

$$\sigma_{\text{intra}}(\omega) \approx \frac{2ie^2}{\pi\hbar^2}\frac{k_BT}{\omega+i\tau^{-1}}\left(\frac{E_f}{2k_BT}\right). \tag{32}$$

The relationship between the Fermi level, E_f, of the graphene sheet and the gate voltage, V_g, in a parallel capacitor configuration can be expressed as

$$E_f = \hbar v_f\sqrt{\pi C_{\text{ox}}/e|V_g - V_{\text{Dirac}}|}, \tag{33}$$

where C_{ox} is the geometric capacitance of the gate oxide and V_{Dirac} is the gate voltage at which minimum conductance is observed. According to (32) and (33), the conductivity of graphene follows a temporal profile proportional to the square root of the modulation voltage. Applying an external bias with a sine-squared waveform such that $E_f = E_{f0}[1 + \beta\sin(\omega_m t + \alpha)]$, the temporal profile of graphene conductivity for an excitation frequency of ω_0 can be written as

$$\sigma(\omega_0,t) = \sigma_{\text{intra}}(\omega_0,E_{f0})\{[1+\beta\sin(\omega_m t+\alpha)]\}. \tag{34}$$

Throughout this paper, the scattering time is considered as $\tau =$ 0.5 ps. Electrical tunability of graphene's Fermi energy level has been demonstrated experimentally in a range of 0–0.6 eV [13]. Here, we have considered $E_{f0} = 0.3$ eV and $\beta = 0.3$ such that the doping level is moderate and within a practical range.

FDTD simulations were carried out using an in-house developed solver, characterizing graphene as a dispersive surface conductivity [62] whose plasma frequency is also modulated in time according to the sinusoidal profile. To model the conformal graphene sheet coating the microwire, a staircase approximation was used [62]. First, the results were compared for different Fermi energy levels and frequencies in the case of unmodulated conductivity. A frequency shift of 0.3 THz was observed in the FDTD results compared to semianalytical solutions as a result of staircasing approximation. This shift is considered in all the FDTD simulations to make a more accurate comparison. The numerical simulation of harmonic generation in time-modulated objects using FDTD requires long time simulations, making it more susceptible to numerical errors. In particular, for modulation frequencies accessible in practice, which are very small compared to the excitation frequency in the THz regime, capturing the steady-state solution will become very challenging and time-consuming. To ensure the accuracy and convergence of FDTD simulations, we consider a modulation frequency of $f_m = f_0/8$. It should be remarked that this modulation frequency may not be accessible in practice and is only considered here for the sake of validation. In all the subsequent analyses and presented applications, we limit ourselves to the experimentally accessible range for the modulation frequency of graphene. The microwires were simulated by applying periodic boundary conditions along the wire axis. A cell size of $\Delta x = \Delta y = \Delta z = 0.5\ \mu$m was used for discretization of the computational domain. The time step was chosen as $\Delta t = 0.925$ fs and the total simulation time was considered as 23 040 time steps ($\approx$21.3 ns). The near-field results were postprocessed in the last four cycles of modulation to obtain generated frequency harmonics through taking the fast Fourier transform (FFT) of time-domain fields. In the semianalytical simulations, the number of cylindrical modes and frequency harmonics were truncated at $M = \pm 3$ and $M_f = \pm 3$ to ensure an almost perfect convergence.

To validate our semianalytical framework, we obtain the near-field results of fundamental and first-order generated harmonics using the FDTD and T-matrix methods for both TE and TM polarizations in two cases of isolated microwires as well as a periodic arrangement of microwires with a periodicity of $\Lambda = 130\ \mu$m. For the sake of brevity, only the near-field results corresponding to the periodic arrangement of microwires incident by a TE-polarized plane wave are included here in Fig. 5, and the rest of the results are presented in Sec. 3 of the Supplemental Material [54]. An excellent agreement is obtained between the results. The mean absolute differences between the results are 3.86%, 6.68%, and 5.49% with respect to the maximum field amplitude for the fundamental, up-modulated, and down-modulated harmonics, respectively. A similar agreement can also be observed for other configurations included in the Supplemental Material, which verifies the validity of our developed theoretical framework. These discrepancies between the two methods are mainly attributed to the FDTD inherent errors and nonidealities, such as a staggered grid for evaluation of field components and finite-time simulations.

We stress that capturing the steady-state response of time-modulated metamaterials in the infrared and optical frequency regimes is very challenging for FDTD simulations due to the small spectral separation between frequency harmonics, which requires long time simulations to be resolved accurately, while the proposed technique gives an analytical solution of the problem and it should yield exact results as long as the modulation-induced dispersion effects are negligible. It is expected that the FDTD results converge to the analytical solution for small modulation frequencies by refining the discretization and increasing the simulation time. In the account of limited computational resources, here we have increased modulation frequency up to $f_m = f_0/8$ and used a total simulation time of $\approx$21.3 ns to successfully perform FDTD simulations and validate our theoretical framework.

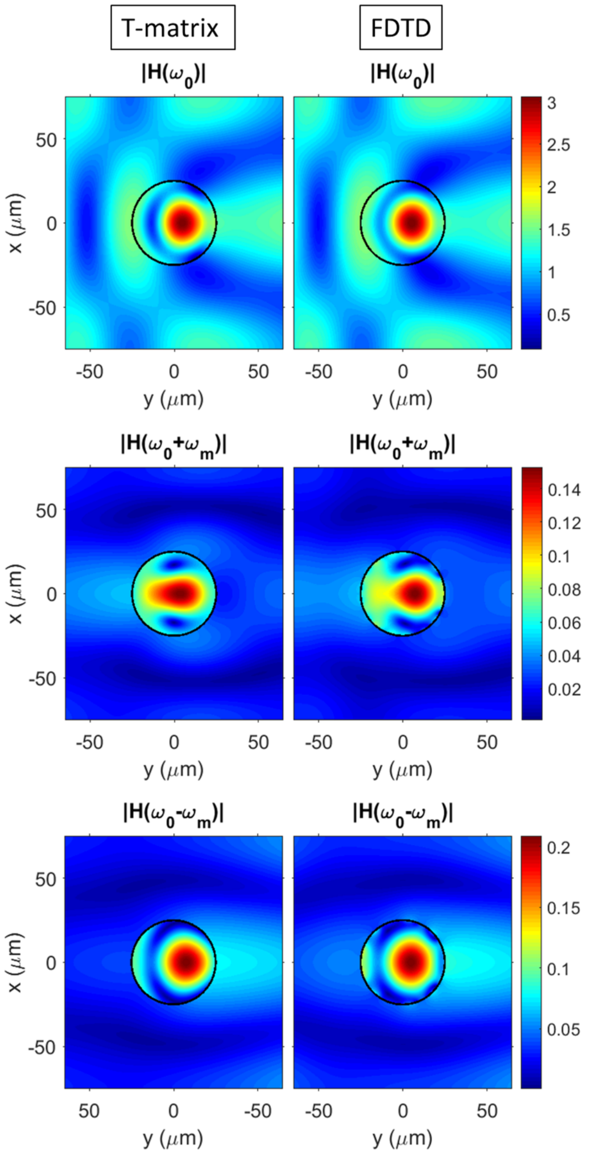

FIG. 5. The comparison of near-field results obtained with the T-matrix and FDTD method corresponding to a periodic array of dielectric cylinders coated by sinusoidally modulated graphene layers incident normally by a TE-polarized plane wave.

The computational statistics of the two methods are compared in Table I for the periodic simulation of microwires. As can be seen, a significant computational gain is afforded by using the semianalytical technique in terms of required memory and computation time. The large required computational resources by FDTD limit its applicability to the analysis of metamaterials, even with a few unit-cells, hindering the fast design of realistic structures. On the contrary, the proposed semianalytical approach can be used efficiently for the simulation of large-area space-time gradient metamaterials. Furthermore, it provides physical insight into the space-time scattering phenomena without the need for costly postprocessing.

III. POTENTIAL APPLICATIONS

Almost all of the previous works on space-time gradient structures focused on exploiting time-reversal asymmetry to develop nonreciprocal components [20–28] such as circulators and insulators, while the capabilities of time-modulated metamaterials in beam-shaping and wavefront engineering of light have remained unexplored thus far. In this section, we

TABLE I. Comparison of computational statistics of the T-matrix and FDTD methods for the periodic simulation of microwires.

Method	Computational time	Memory requirement
T-matrix	15 s	2.6 KB
FDTD	40 min	150 MB

utilize the developed semianalytical framework to explore potential applications of time-modulated metamaterial and metasurface platforms for light manipulation. First, we analyze the dependence of the frequency conversion process to the resonant characteristics of time-modulated building blocks. Then, we establish a systematic design rule for independent control of the amplitude and phase of frequency harmonics in time-modulated metasurfaces, which enables wavefront engineering and holographic generation of frequency harmonics. Finally, we demonstrate the potential of space-time gradient metamaterials for spatiotemporal manipulation of light by designing a time-modulated metalens for beam scanning in time. The presented results provide key physical insights to design time-modulated metamaterials, and they can be generalized and implemented using various time-modulated building blocks with alternative geometries incorporating different electro-optical materials in different frequency regimes.

A. Frequency conversion in time-modulated microwires

To gain more insight into the scattering phenomena from time-modulated antennas, in this section we study the frequency conversion efficiency of a time-modulated graphene-wrapped microwire through analysis of scattering spectra of frequency harmonics. The dependence of the frequency conversion process to the resonant behavior of time-modulated antennas has not been rigorously addressed so far and can provide an intuitive starting point for designing metamaterial platforms consisting of a plurality of such elements.

The frequency conversion can be thought of as a change in the energy of photons due to time modulation, and it is a direct result of temporal variation in the scattering [28,29]. As such, the use of graphene as an electrically tunable material offers a greater advantage in the THz frequency regime, where graphene yields the largest tunability. Furthermore, it is beneficial to integrate graphene into resonant geometries, resulting in larger scattering modulation and higher-frequency conversion efficiency. Here, the topology of the microwire is chosen to meet the following requirements: (i) support Mie resonances in the THz regime, and (ii) allow for electrical biasing of graphene in a parallel capacitor configuration. An n-type silicon microwire with a radius of 40 μm and moderate doping of 10^{15} cm^{-3} coated by a thin insulating layer of SiO$_2$ with a radial thickness of 20 nm is chosen accordingly, as shown in Fig. 6(a). The complex permittivity of silicon is obtained via a Drude model [63] as $\epsilon(\omega) = \epsilon_{\inf} - \frac{\omega_p^2}{\omega^2 + i\omega\Gamma}$ in which $\epsilon_{\inf}$ is the high-frequency permittivity, and ω_p and Γ are the plasma frequency and damping constant, respectively. The plasma frequency is related to carrier concentration (N) through $\omega_p^2 = \frac{Ne^2}{\epsilon_0 m^*}$, in which e is the electron charge, ϵ_0 is the vacuum permittivity, and m^* is the effective mass of an electron. For silicon, we use $\epsilon_{\inf} = 11.7$, $\Gamma = 180$ THz, and $m^* = 0.27 m_e$.

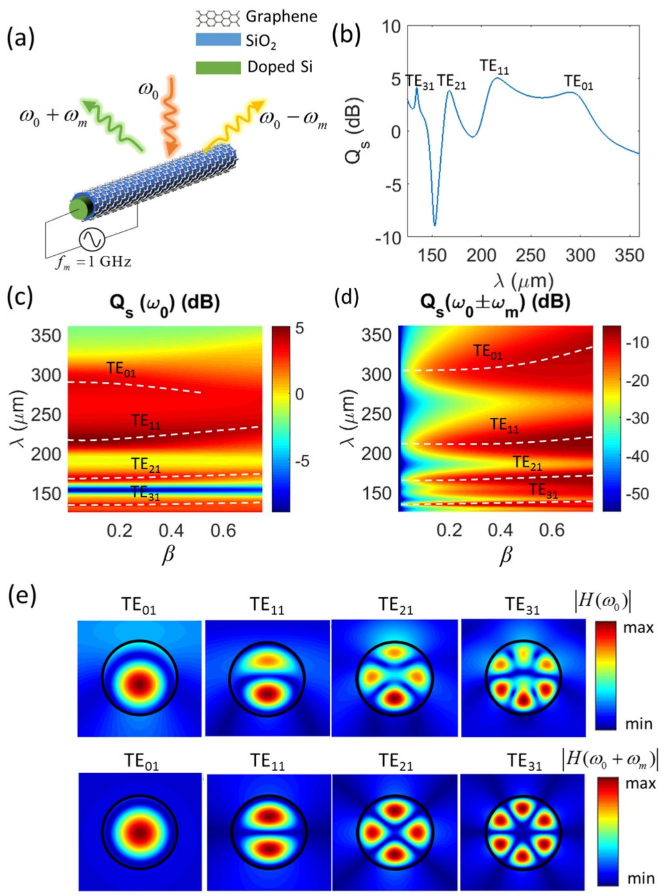

FIG. 6. Frequency conversion in a time-modulated graphene-wrapped microwire. (a) The schematic depiction of a graphene-wrapped Si/SiO$_2$ microwire modulated sinusoidally in time. (b) The TE scattering efficiency spectrum of time-invariant microwire with a Fermi energy level of $E_f = 0.3$ eV. The peaks correspond to TE resonant modes. Parts (c) and (d) represent the scattering efficiencies of the fundamental and first-order generated frequency harmonics as functions of Fermi energy modulation depth and wavelength. (e) The magnetic-field profiles corresponding to the resonant modes of the fundamental and first-order frequency harmonics.

The scattering efficiency of the microwire is demonstrated in Fig. 6(b) as a function of wavelength for time-invariant graphene with a Fermi-energy level of $E_f = 0.3$ eV, incident normally by a TE-polarized plane wave. The peaks in the scattering efficiency spectrum correspond to the TE resonant modes, which are characterized according to their mode profiles. Next, we consider modulating the Fermi energy level sinusoidally with an average value of $E_{f0} = 0.3$ eV. The modulation frequency is chosen as $f_m = 1$ GHz, which is well within the practical range [30]. Furthermore, the generated frequency harmonics can be resolved with the resolution of THz detectors [64]. The extinction coefficients of fundamental and first-order frequency harmonics are demonstrated in Figs. 6(c) and 6(d), respectively, as functions of wavelength and Fermi energy modulation depth. The resonant wavelengths corresponding to the maximal scattering efficiencies are denoted by white dashed lines for each frequency harmonic. As can be observed from the results, the maximum frequency conversion efficiency is obtained in the vicinity of resonant modes of the fundamental frequency harmonic as a result of maximal scattering modulation, while the increase in the modulation depth of the Fermi energy level results in a spectral shift of the resonant modes. Moreover, the frequency conversion efficiency is directly proportional to the modulation depth of the Fermi energy level. It should be noted that, in the account of small modulation frequency, that modulation-induced dispersion effects are negligible and the conversion efficiencies of up- and down-modulated harmonics are almost equal. As the modulation frequency increases, the dispersion effects become more pronounced, which leads to a larger difference between up- and down-modulated harmonics. By changing the modulation frequency in the external bias, the time-modulated microwire can serve as an electrically tunable harmonic generator. Figure 6(e) represents the near-field distributions of the magnetic field corresponding to the resonances of fundamental and first-order frequency harmonics. As can be seen, the mode profiles of the generated frequency harmonic follow the same distribution as those of the fundamental harmonic while being symmetric with respect to the axial direction, which is due to the symmetry and the absence of an incident field component at these frequencies.

It should be mentioned that similar results can be obtained for TM polarization, while the resonant spectra of frequency harmonics will be different due to geometrical asymmetry in orthogonal directions.

B. Time-modulated metasurfaces: Holographic generation of harmonics

Due to the enhanced conversion efficiency associated with resonant features of Mie scattering, graphene-wrapped microwires are ideal candidates for realization of time-modulated metasurfaces. Furthermore, the developed semianalytical technique in this paper allows for a broader exploration of novel space-time scattering phenomena, and it can be used to establish design rules for such emerging paradigms.

Here, we consider a periodic arrangement of graphene-wrapped Si (40 μm)/SiO$_2$ (20 nm) microwires with a subwavelength periodicity of $\Lambda = 130$ μm deposited laterally on a silica substrate with a thickness of 80 μm, incident normally by a TE-polarized plane wave. The Fermi-energy level of graphene is modulated with an offset sinusoid as $E_f = E_{f0}[1 + \beta \sin(\omega_m t + \alpha)]$ with $E_{f0} = 0.3$ eV, and the modulation frequency is assumed to be $f_m = 1$ GHz. Such a metasurface can be implemented by using an active RF biasing grid, which allows for independent addressing and biasing of each microwire. Different modulation depths and phase delays can be achieved by using RF amplifiers and phase shifters [65], respectively. We study the effect of these parameters on the amplitude and phase of generated frequency harmonics to establish a design rule for wavefront engineering in time-modulated metasurfaces.

Figure 7(a) demonstrates the amplitude and phase shift of the transmission coefficients corresponding to the fundamental and first-order frequency harmonics generated by the metasurface, as functions of modulation depth and incident wavelength for a modulation phase delay of $\alpha = 0$. The phase shifts of frequency harmonics are shown as the pseudocolors in the 3D plots. The phase reference at each wavelength is chosen as the phase corresponding to $\beta = 0$ to show more clearly the phase variations with respect to the Fermi energy modulation depth. The dips in the transmission spectrum of the fundamental frequency harmonic correspond to TE resonant modes. As can be seen from the results, the transmission coefficients of generated frequency harmonics exhibit a peak in the vicinity of fundamental harmonic resonant wavelengths due to enhanced scattering modulation. Moreover, the transmission amplitude of generated frequency harmonics increases almost linearly by increments of modulation depth of the Fermi energy while maintaining an almost constant phase at each wavelength. As such, changing the modulation depth of the Fermi energy level can be used for broadband amplitude modulation of generated frequency harmonics.

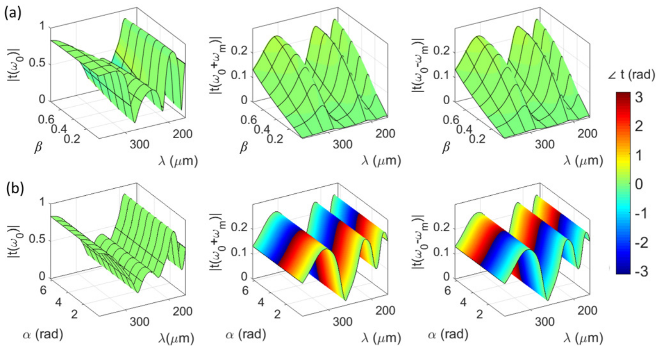

FIG. 7. (a) The amplitude and phase shifts of transmission coefficients corresponding to fundamental and first-order frequency harmonics as functions of wavelength and modulation depth of the Fermi energy for a modulation phase delay of $\alpha = 0$. The phase shift is depicted as pseudocolor and is measured at each wavelength with respect to the phase at $\beta = 0$. Part (b) demonstrates the same quantities as functions of wavelength and modulation phase delay of the Fermi energy for a modulation depth of $\beta = 0.75$. The phase shift at each wavelength is measured with respect to the phase at $\alpha = 0$.

We also study the amplitude and phase shift of the transmission coefficients as functions of modulation phase delay and incident wavelength for a Fermi energy modulation depth of $\beta = 0.75$. The results are presented in 3D plots of Fig. 7(b) in which the phase shift at each wavelength is measured with respect to the phase at $\alpha = 0$. It can be clearly observed from the results that the generated frequency harmonics acquires a phase shift of $\pm\alpha$ while maintaining a constant amplitude at each wavelength. It can be inferred that the light picks up a dispersionless phase shift proportional to the modulation phase delay upon frequency transitions in a time-modulated metasurface while maintaining a constant amplitude. In particular, the phase shifts of up- and down-modulated harmonics are conjugate. In this context, this phase shift closely resembles the dispersionless geometric phase shift, which is introduced by the rotation of elements when the circularly polarized light is undergoing polarization conversion in a half-wave plate while the phase shifts for circular polarizations of opposite handedness are opposite [66,67]. The dispersionless phase shift introduced by modulation phase delay covers a 2π span by electrically tuning the modulation phase delay via

RF phase shifters in biasing. As such, it can be used for broadband wavefront engineering of generated harmonics and realization of different functionalities such as steering and focusing.

It should be noted that similar results can be obtained for reflection of generated harmonics, which are not included here for the sake of brevity. Time-modulated elements are bound to radiate higher-order frequency harmonics on both sides of the metasurface due to symmetry and the absence of an incident field component at these frequencies, unless the transmission is blocked by a backmirror.

The obtained results suggest that independent control over the amplitude and phase of generated harmonics can be achieved by changing the modulation depth and the phase delay, which enables full complex-amplitude modulation and holographic generation of frequency harmonics. This approach is ideal for holography and reconstruction of complex patterns in the nearfields of generated frequency harmonics as the amplitude and phase modulations do not interfere with each other. Moreover, it can address the challenges facing electrically tunable designs based on resonant phase shifts [12–16] suffering from limited phase shift and an extremely narrow bandwidth.

To demonstrate the capability of the proposed approach and the time-modulated metasurface in holographic generation of harmonics, we aim to reconstruct a linear pattern of the first up-modulated frequency harmonic with three flat spots at the intervals of $-12\lambda < x < -6\lambda$, $2\lambda < x < 6\lambda$, and $10\lambda < x < 12\lambda$ at a target plane with a distance of 5λ from the metasurface for an incident wavelength of $\lambda = 300\ \mu\text{m}$ at which the metasurface exhibits an enhanced frequency conversion efficiency. We consider a space-time gradient metasurface consisting of a finite array of 101 identical graphene-wrapped microwires, which are modulated via an RF biasing grid incorporating amplifiers and phase shifters to provide the require modulation depth and phase delay for each element, as shown in Fig. 8(a).

The required amplitude and phase distributions at the metasurface plane are obtained using the fast Fourier transform holography method [7], and they are mapped to the modulation depth and modulation phase delay of the elements, respectively, as shown in Figs. 8(b) and 8(c). The transmitted magnetic-field distribution corresponding to the first up-modulated frequency harmonic is obtained and demonstrated in Fig. 8(d). As can be seen from the results, the pattern is clearly described at the desired location, which indicates that the amplitude profiles are correctly imprinted as well as the phase profiles. Figure 8(e) compares the desired pattern and the realized pattern by the time-modulated metasurface. The edges of flat spots are reconstructed with excellent accuracy. The speckle noise in the flat spots is mainly due to the limited sampling size of the metasurface. It should be noted that the target image is formed in both below and above the metasurface due to the symmetrical radiation of generated frequency harmonics. A similar behavior can be observed for single-layer nonlinear metasurfaces and linear metasurfaces operating at cross-polarization [66–68].

The electrical tunability of the modulation parameters allows for multifunctionality and on-demand manipulation of light. By controlling modulation frequency (f_m), modulation phase delay (α), and modulation depth (β) via RF biasing grid, the metasurface can act simultaneously as a tunable harmonic generator and a manipulator. Furthermore, as demonstrated by the results in Fig. 7, the independent control over the amplitude and phase of generated harmonics can be achieved in a broad range of wavelengths enabling wideband holography. It should be remarked, however, that the frequency conversion efficiency depends on the resonant characteristics of the element, which makes the efficiency dependent on the wavelength and polarization, with the maximum efficiencies obtained in the vicinity of the resonant wavelengths of the fundamental frequency harmonic. In the account of broadband tunability of graphene, the design can be modified to operate in near-IR and mid-IR frequency regimes with a lower frequency conversion efficiency due to the smaller tunability of graphene conductivity.

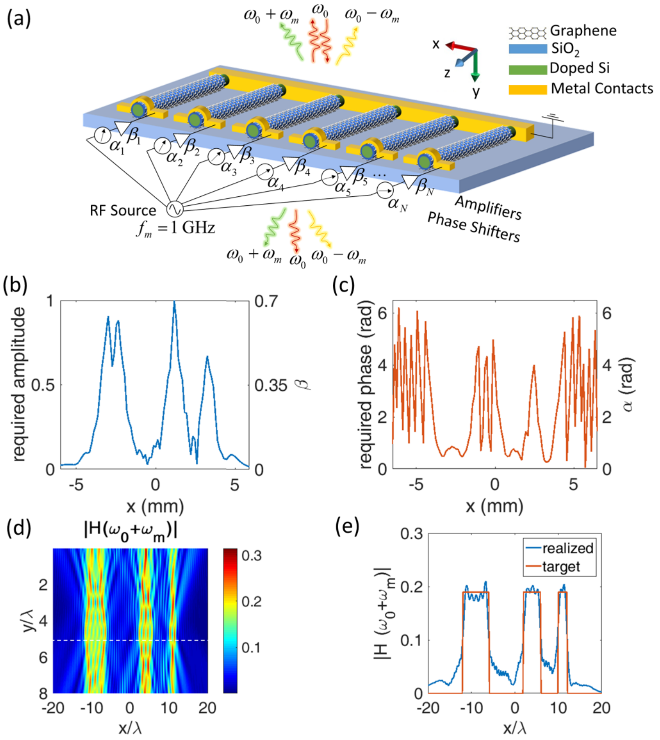

FIG. 8. Holographic generation of frequency harmonics using time-modulated metasurfaces. (a) The schematic of a time-modulated metasurface consisted of graphene-wrapped microwires biased via an active RF circuit incorporating amplifiers and phase shifters to provide required modulation depth and phase delay. Parts (b) and (c) demonstrate the required amplitude and phase modulation at the metasurface plane, respectively, which are mapped to the modulation depth and phase delay of the elements. (d) The magnetic field amplitude corresponding to the first-up modulated frequency harmonic generated in the forward direction (transmission). (e) Comparison of the ideal and realized patterns at the target plane located 5λ away from the metasurface plane.

C. Time-modulated metamaterials: Spatiotemporal control of light

In the nonresonant Mie scattering region (effective medium regime) associated with deeply subwavelength microwires,

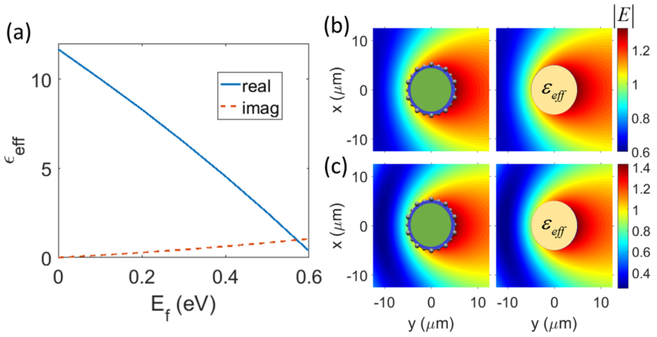

FIG. 9. (a) The effective permittivity of the deeply subwavelength graphene-wrapped microwire as a function of the Fermi energy level of graphene. Parts (b) and (c) compare the near-field distributions of electric field corresponding to graphene-wrapped microwires and homogenized counterparts for Fermi energy levels of $E_f = 0.2$ and 0.5 eV, respectively.

they can be used to realize an effective refractive index by virtue of internal homogenization [3,15,52]. As such, time-modulated graphene-wrapped microwires can be used for realization of space-time gradient metamaterials and photonic crystals [69]. Such platforms offer exciting opportunities for realization of magnetless nonreciprocal optical components [27] as well as spatiotemporal manipulation of light.

As graphene yields a larger tunability at longer wavelengths while exhibiting a lower loss in shorter wavelengths, we choose to operate at $\lambda = 100\ \mu$m to achieve a balanced large tunability and low loss in the effective refractive index of elements. The microwire topology is chosen as Si (5 μm)/SiO$_2$ (10 nm) to be within the effective-medium regime. To demonstrate the applicability of graphene-wrapped microwires as time-modulated building blocks for both polarizations, in this section we consider a TM-polarized incidence. The effective permittivity of the graphene-wrapped microwire is obtained as a function of the Fermi energy level of graphene for a TM-polarized plane wave using a parameter retrieval technique [3,52], and it is shown in Fig. 9(a). A large tunability is achieved for the real part of permittivity while maintaining a relatively small imaginary part by changing the Fermi energy level from 0 to 0.6 eV. To verify the homogenization, we compare the scattering of graphene-wrapped microwire against homogenized counterparts. Figures 9(b) and 9(c) compare the distribution of electric-field magnitude corresponding to the graphene-wrapped microwires with Fermi energy levels of 0.2 eV and 0.5 eV with their homogenized counters, respectively. An excellent agreement is observed between the near-field distributions verifying the validity of the homogenization approach and implying that the graphene-wrapped microwires indeed scatter similarly to the homogenized counters. It should be noted that the field profiles inside the microwires are different for the graphene-wrapped and homogenized microwires.

The results presented in Fig. 9 can be used to implement space-time gradient metamaterials. Here, we aim to design a time-modulated metalens yielding sinusoidal beam-scanning in time such that $\theta = \theta_0 + \Delta\theta \sin(\omega_m t)$ with $f_m = 1$ GHz. This enables ultrafast scanning of light as it affords a period of $\tau = 1$ ns for each scanning cycle. In the static case, a generalized Eaton lens can be used for bending a beam toward an arbitrary refraction angle of θ. The spatial refractive index profile of such a lens can be approximated as [70]

$$n(r) \approx \left(\frac{D_{\text{lens}}}{r} - 1\right)^{\left(\frac{\theta}{\pi+\theta}\right)}, \tag{35}$$

where D_{lens} is the diameter of the lens and r is the radial distance from the center. It should be noted that the singularity of the refractive index profile at the center of the lens and the large required indices limits the applicability of graphene-wrapped Si microwires for achieving large steering angles. By substituting $\theta = \theta_0 + \Delta\theta \sin(\omega_m t)$ into the above equation and assuming $\Delta\theta \ll \pi + \theta_0$, we can obtain

$$\begin{aligned} n(r,t) &\approx \left(\frac{D_{\text{lens}}}{r} - 1\right)^{\left(\frac{\theta_0}{\pi+\theta_0}\right)} \\ &\quad \times \left[1 + \frac{\Delta\theta \sin(\omega_m t)}{\pi + \theta_0} \ln\left(\frac{D_{\text{lens}}}{r} - 1\right)\right] \\ &= n_{\text{avg}}(r) + \Delta n \sin(\omega_m t). \end{aligned} \tag{36}$$

According to (36), a sinusoidal beam-steering can be achieved by a sinusoidal modulation of the refractive index profile when the steering range is small ($\Delta\theta \ll \pi + \theta_0$). The space-time gradient metamaterial can be implemented by vertical deposition of microwires on a substrate, which can be addressed and biased independently from the top using an RF biasing grid incorporating amplifiers to provide the required modulation depth and offset for each element, as shown schematically in Fig. 10(a).

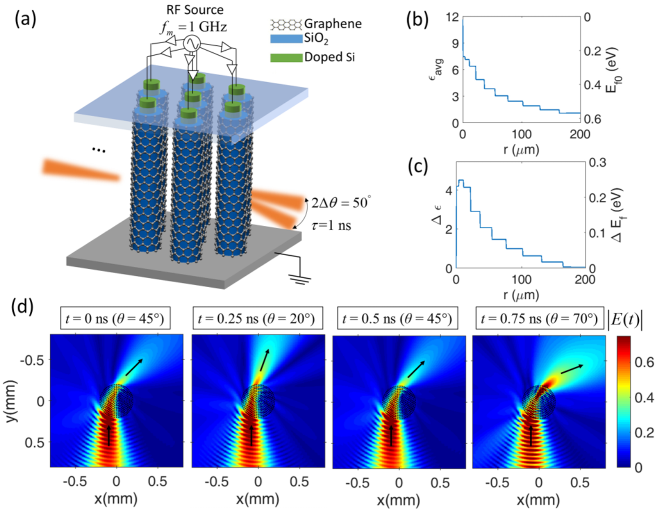

FIG. 10. Spatiotemporal manipulation of light using a time-modulated metamaterial. (a) The schematic depiction of a space-time gradient metamaterial consisted of graphene-wrapped microwires biased from the top using an RF biasing grid incorporating amplifiers to provide required modulation depth and offset for each element. Parts (b) and (c) demonstrate the required average value and modulation depth of the effective permittivity, respectively, as functions of the radial position within the lens, which are mapped to the average value and modulation depth of the Fermi energy of graphene-wrapped microwires. (d) The steady-state electric-field amplitude distribution at different time steps within a scanning cycle.

We use a circular array of 331 microwires arranged in 11 layers with an edge-to-edge separation distance of 10 μm forming a circular lens with a diameter of $D_{\text{lens}} = 4\lambda = 400\ \mu$m. The filling fraction in this case is FF ≈ 0.2 and the sampling period in the radial direction is 20 μm ($\lambda/5$), which is within the effective-medium regime. The lens is incident by a TM-polarized Gaussian beam with a waist of $D_y/4 = \lambda$ and an offset of $x_0 = D_y/4$ with respect to the center of the lens. We choose $\theta_0 = 45^\circ$ and $\Delta\theta = 25^\circ$ and obtain the required average value and modulation depth of the effective permittivity of microwires using (36) based on the effective-medium theory as functions of radial position within the lens. Using the presented results in Fig. 9, the values are then mapped into the average value and modulation depth of graphene-wrapped microwires, as shown in Figs. 10(b) and 10(c).

The structure is solved using the proposed semianalytical framework, and the steady-state time-domain solution is obtained by taking the inverse Fourier transform of the frequency response. The frequency harmonics are considered up to $M_f = \pm 4$ in simulations to ensure the convergence of the results. Figure 10(d) demonstrates the electric-field amplitude at different time steps within a cycle of modulation. The results verify the ultrafast beam scanning achieved in the steering range set by the design. The temporal scanning of the beam can be seen more clearly in the movie provided as Supplemental Material [54]. The presented design illustrates the great promise of time-varying metamaterials for spatiotemporal manipulation of light. A more rigorous design approach can be established by extending generalized field transformations into the time domain and employing temporal variations beyond the sinusoidal modulation profile.

IV. CONCLUSION

A robust semianalytical framework was developed based on a transition-matrix formulation that is able to efficiently characterize the near-field and far-field scattering from periodic and aperiodic arrangements of time-varying graphene-wrapped wire elements on top of layered substrates. The method was verified by comparing the results with full-wave FDTD simulations. A significant computational gain was afforded by the method, which enables fast design of space-time gradient metamaterials with advanced functionalities. It was applied to establish novel design rules for time-modulated metamaterial platforms and explore their potential applications in frequency conversion, holographic generation of frequency harmonics, and spatiotemporal manipulation of light. Our finding can foster the design of time-modulated metamaterials with different geometries and tunable materials in different frequency regimes, enabling novel and improved functionalities.

ACKNOWLEDGMENT

This work is supported in part by the U.S. Air Force Office of Scientific Research (AFOSR), FA9550-14-1-0349.

---

[1] H. Chen, C. T. Chan, and P. Sheng, Nat. Mater. **9**, 387 (2010).

[2] H.-T. Chen, A. J. Taylor, and N. Yu, Rep. Prog. Phys. **79**, 076401 (2016).

[3] C. Della Giovampaola and N. Engheta, Nat. Mater. **13**, 1115 (2014).

[4] N. Yu and F. Capasso, Nat. Mater. **13**, 139 (2014).

[5] F. Aieta, P. Genevet, M. A. Kats, N. Yu, R. Blanchard, Z. Gaburro, and F. Capasso, Nano Lett. **12**, 4932 (2012).

[6] M. Farmahini-Farahani and H. Mosallaei, Opt. Lett. **38**, 462 (2013).

[7] X. Ni, A. V. Kildishev, and V. M. Shalaev, Nat. Commun. **4**, 2807 (2013).

[8] J.-Y. Ou, E. Plum, J. Zhang, and N. I. Zheludev, Nat. Nanotechnol. **8**, 252 (2013).

[9] N. I. Zheludev and E. Plum, Nat. Nanotechnol. **11**, 16 (2016).

[10] A. Tittl, A.-K. U. Michel, M. Schäferling, X. Yin, B. Gholipour, L. Cui, M. Wuttig, T. Taubner, F. Neubrech, and H. Giessen, Adv. Mater. **27**, 4597 (2015).

[11] Z. Zhu, P. G. Evans, R. F. Haglund Jr., and J. G. Valentine, Nano Lett. **17**, 4881 (2017).

[12] Y.-W. Huang, H. W. H. Lee, R. Sokhoyan, R. A. Pala, K. Thyagarajan, S. Han, D. P. Tsai, and H. A. Atwater, Nano Lett. **16**, 5319 (2016).

[13] M. C. Sherrott, P. W. Hon, K. T. Fountaine, J. C. Garcia, S. M. Ponti, V. W. Brar, L. A. Sweatlock, and H. A. Atwater, Nano Lett. **17**, 3027 (2017).

[14] J. Park, J.-H. Kang, S. J. Kim, X. Liu, and M. L. Brongersma, Nano Lett. **17**, 407 (2016).

[15] M. M. Salary and H. Mosallaei, Sci. Rep. **7**, 10055 (2017).

[16] A. Forouzmand and H. Mosallaei, J. Opt. **18**, 125003 (2016).

[17] Y. Yao, R. Shankar, M. A. Kats, Y. Song, J. Kong, M. Loncar, and F. Capasso, Nano Lett. **14**, 6526 (2014).

[18] J. R. Zurita-Sánchez, P. Halevi, and J. C. Cervantes-Gonzalez, Phys. Rev. A **79**, 053821 (2009).

[19] J. R. Zurita-Sánchez and P. Halevi, Phys. Rev. A **81**, 053834 (2010).

[20] H. Lira, Z. Yu, S. Fan, and M. Lipson, Phys. Rev. Lett. **109**, 033901 (2012).

[21] Z. Yu and S. Fan, Nat. Photon. **3**, 91 (2009).

[22] Y. Hadad, D. L. Sounas, and A. Alu, Phys. Rev. B **92**, 100304(R) (2015).

[23] S. Taravati, N. Chamanara, and C. Caloz, Phys. Rev. B **96**, 165144 (2017).

[24] N. Chamanara, S. Taravati, Z.-L. Deck-Léger, and C. Caloz, Phys. Rev. B **96**, 155409 (2017).

[25] S. Taravati, B. A. Khan, S. Gupta, K. Achouri, and C. Caloz, IEEE Trans. Antennas Propag. **65**, 3589 (2017).

[26] S. Taravati and C. Caloz, IEEE Trans. Antennas Propag. **65**, 442 (2017).

[27] D. L. Sounas and A. Alù, Nat. Photon. **11**, 774 (2017).

[28] A. Shaltout, A. Kildishev, and V. Shalaev, Opt. Mater. Express **5**, 2459 (2015).

[29] Z. Liu, Z. Li, and K. Aydin, ACS Photon. **3**, 2035 (2016).

[30] C. T. Phare, Y.-H. D. Lee, J. Cardenas, and M. Lipson, Nat. Photon. **9**, 511 (2015).

[31] M. Liu, X. Yin, E. Ulin-Avila, B. Geng, T. Zentgraf, L. Ju, F. Wang, and X. Zhang, Nature (London) **474**, 64 (2011).

[32] N. Youngblood, Y. Anugrah, R. Ma, S. J. Koester, and M. Li, Nano Lett. **14**, 2741 (2014).

[33] M. Mohsin, D. Schall, M. Otto, A. Noculak, D. Neumaier, and H. Kurz, Opt. Express **22**, 15292 (2014).

[34] C. Qiu, W. Gao, R. Vajtai, P. M. Ajayan, J. Kono, and Q. Xu, Nano Lett. **14**, 6811 (2014).

[35] G. Larrieu and X.-L. Han, Nanoscale **5**, 2437 (2013).

[36] K. Storm, G. Nylund, L. Samuelson, and A. P. Micolich, Nano Lett. **12**, 1 (2011).

[37] R. Wang, Y. Hao, Z. Wang, H. Gong, and J. T. Thong, Nano Lett. **10**, 4844 (2010).

[38] Y. Wu, B. Yao, A. Zhang, Y. Rao, Z. Wang, Y. Cheng, Y. Gong, W. Zhang, Y. Chen, and K. Chiang, Opt. Lett. **39**, 1235 (2014).

[39] W. Li, B. Chen, C. Meng, W. Fang, Y. Xiao, X. Li, Z. Hu, Y. Xu, L. Tong, H. Wang *et al.*, Nano Lett. **14**, 955 (2014).

[40] C. Zhang, L. Tu, Z. Huang, L. Liu, P. Zhan, C. Sun, and Z. Wang, J. Opt. **18**, 125007 (2016).

[41] P.-Y. Chen and A. Alù, ACS Nano **5**, 5855 (2011).

[42] A. R. Davoyan and N. Engheta, ACS Photon. **3**, 737 (2016).

[43] Y. Gao and I. V. Shadrivov, Opt. Lett. **41**, 3623 (2016).

[44] P. Waterman, Proc. IEEE **53**, 805 (1965).

[45] B. Peterson and S. Ström, Phys. Rev. D **8**, 3661 (1973).

[46] W. C. Chew and W. C. Chew, *Waves and Fields in Inhomogeneous Media* (IEEE, New York, 1995), Vol. 522.

[47] H. Roussel, W. Chew, F. Jouvie, and W. Tabbara, J. Electromagn. Waves. Appl. **10**, 109 (1996).

[48] K. Yasumoto, H. Toyama, and T. Kushta, IEEE Trans. Antennas Propag. **52**, 2603 (2004).

[49] H. Toyama and K. Yasumoto, Progr. Electromagn. Res. **52**, 321 (2005).

[50] M. M. Salary, M. Nazari, and H. Mosallaei, J. Opt. Soc. Am. B **32**, 2448 (2015).

[51] M. M. Salary, S. Jafar-Zanjani, and H. Mosallaei, Progr. Electromagn. Res. B **72**, 31 (2017).

[52] S. Jafar-Zanjani, M. M. Salary, and H. Mosallaei, ACS Photon. **4**, 915 (2017).

[53] D. Wright and R. Cobbold, Smart Mater. Struct. **19**, 045006 (2010).

[54] See Supplemental Material at http://link.aps.org/supplemental/10.1103/PhysRevB.97.115421 for further details on technical implementation of the method, expressions for the time-varying aggregate T-matrix, near-field comparisons with full-wave FDTD simulations, and the movie showing beam scanning in time.

[55] T.-H. Xiao, L. Gan, and Z.-Y. Li, Opt. Express **23**, 18975 (2015).

[56] R. Borghi, M. Santarsiero, F. Frezza, and G. Schettini, J. Opt. Soc. Am. A **14**, 1500 (1997).

[57] R. Borghi, F. Frezza, C. Santini, G. Schettini, and M. Santarsiero, J. Electromagn. Waves Appl. **13**, 27 (1999).

[58] R. Borghi, F. Frezza, M. Santarsiero, C. Santini, and G. Schettini, J. Electromagn. Waves Appl. **14**, 1353 (2000).

[59] A. Vakil and N. Engheta, Science **332**, 1291 (2011).

[60] M. M. Salary and H. Mosallaei, Phys. Rev. B **94**, 035410 (2016).

[61] S. Rakheja and P. Sengupta, IEEE Trans. Nanotechnol. **15**, 113 (2016).

[62] S. Jafar-Zanjani, J. Cheng, and H. Mosallaei, Appl. Opt. **55**, 2967 (2016).

[63] G. V. Naik, V. M. Shalaev, and A. Boltasseva, Adv. Mater. **25**, 3264 (2013).

[64] T. Yasui, Y. Kabetani, E. Saneyoshi, S. Yokoyama, and T. Araki, Appl. Phys. Lett. **88**, 241104 (2006).

[65] E. A. Firouzjaei, *mm-Wave Phase Shifters and Switches* (University of California Press, Berkeley, CA, 2010).

[66] X. Chen, L. Huang, H. Mühlenbernd, G. Li, B. Bai, Q. Tan, G. Jin, C.-W. Qiu, S. Zhang, and T. Zentgraf, Nat. Commun. **3**, 1198 (2012).

[67] M. Tymchenko, J. S. Gomez-Diaz, J. Lee, N. Nookala, M. A. Belkin, and A. Alù, Phys. Rev. B **94**, 214303 (2016).

[68] S. Keren-Zur, O. Avayu, L. Michaeli, and T. Ellenbogen, ACS Photon. **3**, 117 (2015).

[69] L. Zeng, J. Xu, C. Wang, J. Zhang, Y. Zhao, J. Zeng, and R. Song, Sci. Rep. **7**, 17165 (2017).

[70] S.-H. Kim, J. Mod. Opt. **59**, 839 (2012).